Elastic wave velocity changes due to the fracture aperture and density, and direct correlation with permeability: an energetic approach to mated rock fractures

K. Sawayama[1], T. Ikeda[2,3], T. Tsuji[2,3,4], F. Jiang[2,5,6], O. Nishizawa[2], and Y. Fujimitsu[3]

[1]Department of Earth Resources Engineering, Graduate School of Engineering, Kyushu University, Fukuoka, Japan

[2]International Institute for Carbon-Neutral Energy Research, Kyushu University, Fukuoka, Japan

[3]Department of Earth Resources Engineering, Faculty of Engineering, Kyushu University, Fukuoka, Japan

[4]Disaster Prevention Research Institute, Kyoto University, Uji, Japan

[5]Department of Mechanical Engineering, Graduate School of Sciences and Technology for Innovation, Yamaguchi University, Ube, Japan

[6]Blue Energy Center for SGE Technology (BEST), Yamaguchi University, Ube, Japan

Corresponding author: Kazuki Sawayama (k.sawayama0926@mine.kyushu-u.ac.jp)

Key Points:

- A numerical approach based on internal energy calculations was developed to calculate precise velocity changes with fracture opening.
- Velocity can be accounted for by superposition of a linear function of the fracture density and quadratic function of the aperture size.
- Normalized velocity has a linear relationship with normalized permeability, and the trend depends on fracture density.

Abstract

In an effort to reveal the subsurface hydraulic changes in fractures by seismic monitoring, aperture-related velocity changes need to be investigated. We developed a numerical approach for calculating changes in elastic wave velocity with fracture aperture opening by determining the internal energy of a digitized fracture model based on natural rough surfaces. The simulated local elastic energy revealed that the interaction energy converged within 1.5 mm of the mean fracture position, and was insignificant unless the fractures intersected. This energetic approach clarified the aperture–velocity relationship and reproduced the experimental results. Further calculations using digital fractures with various sizes and density demonstrated that the velocity can be accounted for by the superposition of a linear function of fracture density and quadratic function of aperture, and is insensitive to the fracture size. Although the relationship

between fracture permeability and elastic wave velocity (i.e., the k–V relationship) depends on the fracture density, the offset-normalized k–V relationship shows clear linearity with the fracture density. The proposed k–V relationship as a function of the aperture and fracture density indicates that laboratory-scale fracture properties of a single fracture can be applied to multiple fractures on a larger scale. Our findings can be used to interpret temporal changes in seismic observations and to monitor fluid flow in fractures.

Plain Language Summary

A monitoring of seismic velocity will be useful to find changes in the permeability of fractures, if the relationship between elastic wave velocity and fracture aperture is known. This study presents a numerical approach to calculating changes in elastic wave velocity, based on the elastic energy calculated using a digital rock model having simulated natural fractures. The proposed approach revealed the relationship between fracture aperture and elastic wave velocities propagating through the fracture. Further calculations showed linear decreases of wave velocities with the number of fractured layers per unit thickness (i.e., the fracture density), whereas the velocities do not significantly change with fracture size. Our results will allow us to formulate the relationship between fracture permeability and elastic wave velocity as a function of fracture density. The proposed equation suggests that the properties of a single fracture on the laboratory scale can be used for a large-scale multiple fracture system. The results will provide a prospective application of seismic data to be used in the sustainable development of fractured reservoirs such as geothermal resources.

1. Introduction

Monitoring fracture systems is important in geology and geophysics, because fractures control mass and heat transport in the subsurface, which are linked to earthquakes (i.e., the fault valve model; Sibson et al., 1988) and fractured reservoir management (e.g., Manga et al., 2012). Recent advances in seismic monitoring techniques have revealed changes in elastic wave velocity associated with earthquakes (e.g., Brenguier et al., 2008; Nimiya et al., 2017) and geothermal fluid production (Sánchez-Pastor et al., 2019; Taira et al., 2018). These velocity changes in the vicinity of a fractured zone will reflect subsurface stress changes that also cause changes in the contact state of fractures (i.e., apertures or asperities). Numerous experimental and numerical studies of fractured rock masses have revealed that aperture networks are strongly related to hydraulic properties, whereas asperity contacts contribute to elastic properties (Guéguen & Boutéca, 2004; Guéguen & Palciauskas, 1994; Ishibashi et al., 2015; Nolte et al., 1989; Sawayama et al., 2021a). An aperture increase or contact area decrease triggered by a subsurface stress change will cause both an increase in permeability and a decrease in elastic constants. Therefore, the hydraulic and elastic properties may be related reflecting changes in the microstructures of the fractures (i.e., apertures and asperities). Previous studies have reported a correlation between permeability and fracture specific stiffness, which is related to the amplitude of the seismic response (i.e., attenuation), but have not

established a direct correlation between permeability and elastic wave velocity (Pyrak-Nolte & Nolte, 2016; Wang & Cardenas, 2016). A direct correlation would be beneficial for evaluating changes in subsurface fracture flow by seismic velocity monitoring.

The fracture permeability k is commonly described by the aperture d as $k = d^2/12$ in the classical parallel plate model (e.g., Witherspoon et al., 1980). It can be linked to the elastic wave velocity if the aperture–velocity relationship is known. However, no established model has correlated these parameters. Although some experimental studies have reported a velocity increase in fractured rock masses at elevated stress (e.g., Nara et al., 2011; Kurtuluş et al., 2012; Yang et al., 2019), evaluating actual changes in the apertures is not feasible by experimental studies. As such, it is important to study the elastic wave velocity of a fractured rock mass by numerical simulations, while changing the aperture between two rough surfaces. A numerical approach allows the S-wave velocity to be calculated even at lower stresses (i.e., a larger aperture), which could then be used to interpret the velocity changes in the upper crust inferred from cross-correlation of ambient noise (e.g., Brenguier et al., 2008; Ikeda & Tsuji, 2018; Nimiya et al., 2017; Sánchez-Pastor et al., 2019; Taira et al., 2018).

To determine the aperture–velocity relationship of a fractured rock mass, this study developed a numerical method that calculates anisotropic elastic constants (i.e., the stiffness tensor C_{ijkl}) based on an internal energy calculation using the finite element method (FEM). The finite element analysis of static elasticity has been used to determine the elastic wave velocity in digitized rock images (e.g., Andrä et al., 2013; Sain et al., 2014). These conventional FEM approaches can only calculate effective elastic constants in a purely isotropic case under isostrain conditions (i.e., the upper bound). The energetic approach makes it possible to calculate the stiffness tensor of vertical transverse isotropic (VTI) media. We also implemented the constant stress assumption in the numerical self-consistent scheme (Nishizawa, 1982) to mitigate the overestimation of elastic constants using the conventional FEM approach. We first applied our approach to synthetic rough fractures based on the natural rough surfaces in contact, and then undertook calculations with aperture opening to estimate the changes in elastic wave velocity during deformation. The calculations were extended to fractures with different sizes and densities. After the experimental verification, we demonstrate that there is a possible correlation with fracture permeability, which highlights an application of our approach.

2. Energy of fractured rock according to elasticity theory

The elastic field of a composite medium comprising a homogeneous matrix and inclusions was described by Eshelby (1957). Let E_0 be the elastic energy of an intact material when it is free of inhomogeneities and under certain surface loads which produce an internal stress field corresponding to the surface stress ${\sigma_{\mathrm{ij}}}^A$. In what follows, we consider the isothermal condition. If we introduce inhomogeneity with keeping ${\sigma_{\mathrm{ij}}}^A$ constant, the elastic energy is augmented by $-E_{\mathrm{int}}({\sigma_{\mathrm{ij}}}^A)$, which represents the interaction energy of the applied stress and the inhomo-

geneities in the medium. If such a process is at constant load (i.e., isostress conditions), then the total energy associated with inclusions is described by the Gibbs free energy G as:

$$G = \frac{1}{2} {C_{ijkl}}^{-1} {\sigma_{ij}}^{A} {\sigma_{kl}}^{A} = E_0 - E_{int}({\sigma_{ij}}^{A}).\#(1)$$

where C_{ijkl} is the stiffness tensor and ${C_{ijkl}}^{-1}$ is its inverse and termed the elastic compliance tensor. The same elastic energy E_0 can be obtained as a function of the surface strain ${\varepsilon_{ij}}^{A}$, corresponding to the surface displacements that are produced by the same surface loads. When the inhomogeneities are introduced, the interaction energy is augmented by $E_{int}({\varepsilon_{ij}}^{A})$, leading to the Helmholtz free energy F:

$$F = \frac{1}{2} C_{ijkl} {\varepsilon_{ij}}^{A} {\varepsilon_{kl}}^{A} = E_0 + E_{int}({\varepsilon_{ij}}^{A}).\#(2)$$

Eshelby (1957) proposed an analytical solution for E_{int} using the eigen or stress-free strain ${\varepsilon_{kl}}^{T}$, by assuming an elliptical inclusion that is often modeled as cracks (Nishizawa, 1982; Nishizawa & Kanagawa, 2010; Yamamoto et al., 1981). However, the complex shapes of fracture apertures cannot be modeled as cracks, and prevented us from analytically calculating E_{int}. We directly calculated F as:

$$F = \frac{1}{2} \iiint_V \sigma_{ij}(x,y,z) \varepsilon_{ij}(x,y,z) dxdydz,\#(3)$$

where V is the volume of the material, and $\sigma_{ij}(x,y,z)$ and $\varepsilon_{ij}(x,y,z)$ are the stress and strain at a point (x, y, z) in the material. C_{ijkl} is defined as the second derivative of F:

$$C_{ijkl} = \frac{\partial^2 F}{\partial {\varepsilon_{ij}}^{A} \partial {\varepsilon_{kl}}^{A}}.\#(4)$$

The conventional FEM calculation solves for the microscopic stress and strain according to an arbitrarily input macroscopic strain ${\varepsilon_{ij}}^{A}$. We approximated F in the FEM by discretizing Eq. (3). However, a constant value of ${\varepsilon_{ij}}^{A}$ will yield C_{ijkl} in the isostrain case (upper bound). To incorporate the constant stress assumption into the conventional FEM, we adopted the numerical self-consistent (NSC) scheme (Le Ravalec & Guéguen, 1996a, 1996b; Nishizawa & Kanagawa, 2010; Yamamoto et al., 1981). In this approach, ${\varepsilon_{ij}}^{A}$ was updated in a stepwise fashion to keep the initially assumed macroscopic stress ${\sigma_{ij}}^{ini}$ constant with increasing mean aperture. The iterative process is described as:

$${\varepsilon_{kl}}^{A(n)} = {C_{ijkl}^{(n-1)}}^{-1} {\sigma_{ij}}^{ini}, \#(5)$$

where the superscripts n or $(n-1)$ of ${\varepsilon_{\mathrm{kl}}}^{A}$ and C^{-1}_{ijkl} denote the values of the nth or $(n-1)$th step. This integrated approach using FEM and NSC methods enables us to solve reasonable changes in the anisotropic form of C_{ijkl}, which is not feasible with a conventional FEM approach. Given that a jointed rock can be assumed to be transversely isotropic along the z-axis (i.e., perpendicular to the fracture plane), the objective C_{ijkl} has a hexagonal symmetry (Mavko et al., 2009):

$$C_{\mathrm{ijkl}} = \begin{bmatrix} C_{1111} & C_{1122} & C_{1133} & 0 & 0 & 0 \\ C_{1122} & C_{1111} & C_{1133} & 0 & 0 & 0 \\ C_{1133} & C_{1133} & C_{3333} & 0 & 0 & 0 \\ 0 & 0 & 0 & C_{1212} & 0 & 0 \\ 0 & 0 & 0 & 0 & C_{1212} & 0 \\ 0 & 0 & 0 & 0 & 0 & \frac{C_{1111}-C_{1122}}{2} \end{bmatrix} . \#(6)$$

3. Data and Method

3.1. Sample and digitization

We prepared digital models of a fractured rock mass from natural rough surfaces, which were also used in Sawayama et al. (2021b) for calculating fracture permeability as a function of the fracture aperture. The surface topography of a natural rock fracture was initially mapped using a laser profilometer (Keyence, VR-3050) with a grid of cells 23.433 µm square. This raw data for the natural rough surfaces were used to further validate our approach (Section 3.3). We then analyzed the fractal characteristics of the natural rough surfaces, obtaining a fractal dimension D = 2.4, roughness s = 0.49, and mismatch length scale $\lambda_c = 0.57$ mm (see Sawayama et al., 2021b for details of this analysis). Based on these values, we constructed a synthetic fracture that was 24 × 24 mm in size with an isotropic surface topography by applying fractional Brownian motion (Brown, 1995; Matsuki et al., 2006; Sawayama et al., 2021b). This method can reproduce a self-similar fracture surface with the same amplitude and a different relative phase for each fracture surface, where the matedness at wavelengths larger than λ_c and a mismatch at smaller wavelengths were modeled. The obtained topographies of the hanging wall and footwall are shown in Fig. 1a and b, respectively. A 3D fracture model was then created numerically by pairing these surfaces (Fig. 1c). The aperture of the model was varied by uniformly reducing the local apertures (Fig. 1d and e). Finally, we prepared 16 models that have different mean apertures (d = 0.05–0.2 mm) with a grid size of 0.1 mm. Although the elastic properties calculated from the FEM are potentially affected by the model grid size (Arns et al., 2002), the 0.1 mm grid size was confirmed to be detailed enough for our approach (Text S1 and Fig. S1). The thickness of the base models is 10 mm, which provides 0.5%–2.0% of the porosity variation.

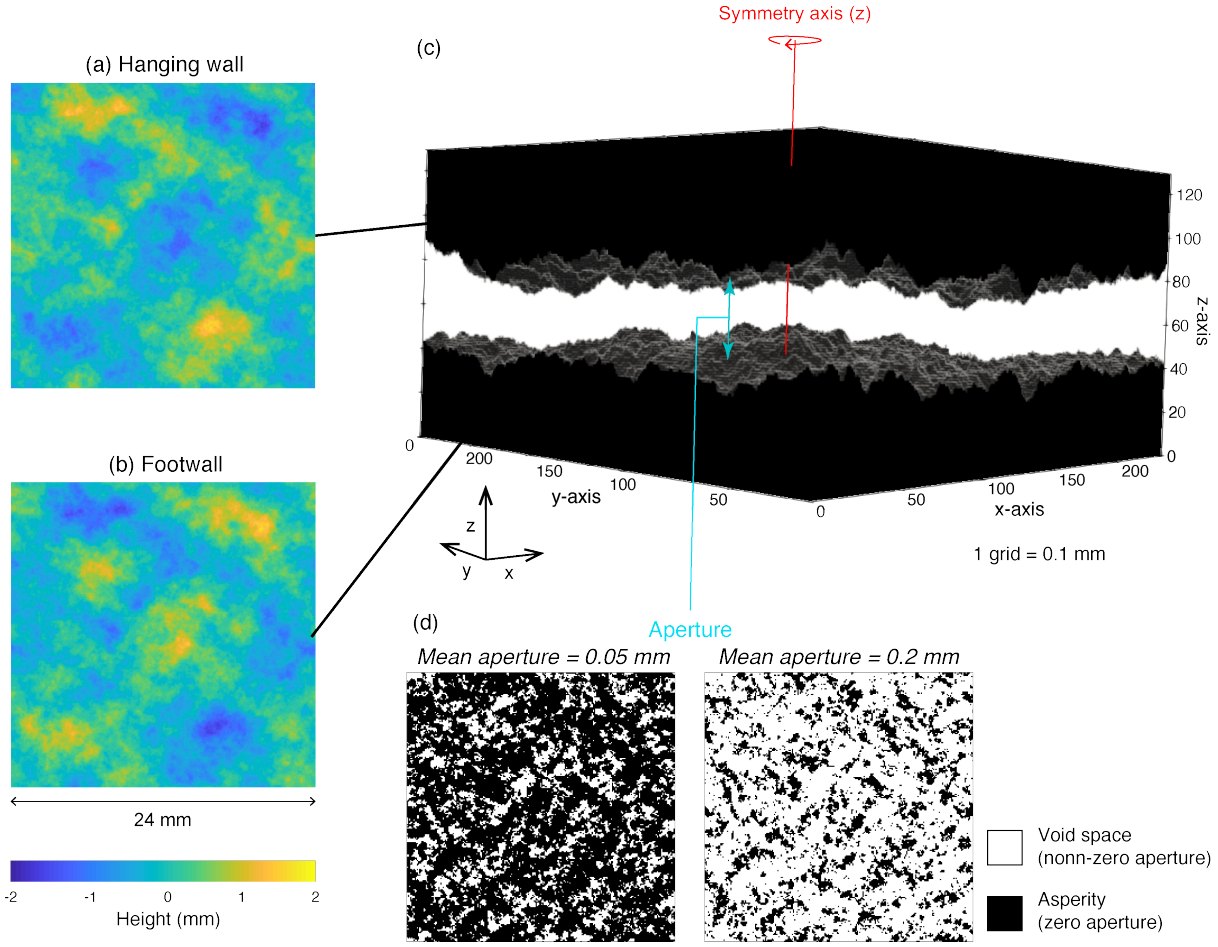

Figure 1. Topography maps of the (a) hanging wall and (b) footwall of the synthetic fracture. (c) Three-dimensional view of the digital fracture model. (d) Asperity distributions of digital fracture models having a different mean aperture.

3.2. Fracture upscaling and multiplication

It is well known that fracture roughness (i.e., the standard deviation of the surface height) increases with fracture length. This study incorporated this scaling law into our model as follows (Matuski et al., 2006):

$$s = s_0 \left(\frac{L}{L_0}\right)^{3-D}, \#(7)$$

where s_0 is the standard deviation of the surface height along a linear profile of size L_0 on a fracture surface and s is the standard deviation of the surface height of an arbitrary fracture size L. In this study, we used $L_0 = 24$ mm and

s_0 = 0.49 mm from our results for the natural rock fracture, and generated three different fracture sizes (L = 24, 48, and 96 mm). The reconstruction of the surface roughness of a fracture from an observed spectrum is a stochastic process, and thus we needed to examine stochastic fluctuations in the models created by different random seeds. This study used five different random seeds to validate the repeatability of our simulation results for each fracture size.

The multiple fracture models were constructed by assuming a vertical series of single fractures having the same aperture value. We selected 1.5 mm as the distance between two single-aligned fractures (i.e., the fracture spacing), because the interaction energy almost converged at this distance. When the fracture spacing was smaller than this distance, the energy anomalies near the fracture planes interfere with each other, resulting in a higher energy peak than the model with a 3.0 mm fracture spacing (Fig. S2). We prepared up to five-layered fractures with 1.5 mm spacing that were each 10 mm in thickness (i.e., fracture density D_F = 1–5 cm^{-1}).

3.3. Anisotropic elastic constants of fractured rock determined by finite-element analysis

Based on Eshelby's theory, an embedded transverse fracture (i.e., inclusion) in the model (Fig. 1c) augments the internal energy (i.e., Helmholz free energy F), which is more significant as the aperture opens. This study analyzed quasi-static changes in F by modifying the conventional FEM approach (Arns et al., 2002; Garboczi, 1998; Sawayama et al., 2021a). In the analysis, we imposed a periodic boundary in all directions, which simulates an infinitely large model with a constant fracture density in a vertical direction (i.e., the number of fractures per unit thickness). The base model has a single fracture in a 10 mm thick layer, and the fracture density D_F = 1 cm^{-1}. The elastic constants we assigned in each solid and fluid node for the FEM are listed in Table 1, based on P- and S-wave velocity (6.04 km/s and 3.33 km/s) under a high confining pressure.

The workflow of the modified FEM is shown in Fig. 2, which comprises three iteration steps: the conjugate gradient, isostress, and NSC steps. The calculation begins with the smallest aperture model (d = 0.05 mm). We first used a homogeneous ${\varepsilon_{\mathrm{kl}}}^A$, where we assumed an isotropic C_{ijkl} for the intact rock ($C_{1111} = C_{3333} = K_s + 4/3\ \mu_s$, $C_{1212} = (C_{1111} - C_{1122})/2 = \mu_s$, and $C_{1122} = C_{1133} = K_s - 2/3\mu_s$, where K_s and μ_s are the bulk and shear moduli of the solid phase, respectively) and ${\sigma_{\mathrm{ij}}}^{\mathrm{ini}}$ = 20 MPa in Eq. (5). Although the actual stress–strain state is heterogeneous due to the presence of the fracture, we first neglected the small error on the energy calculation caused by this assumption for convenience. The local internal energy was calculated by the FEM, which was repeated to minimize the gradient of F with respect to the displacement by the conjugate gradient iteration (Fig. 2a). After the convergence, C_{ijkl} can be solved with Eq. (4). We numerically differentiated F with respect to ${\varepsilon_{\mathrm{ij}}}^A$ by assuming the vertical transverse isotropy (VTI) of the fractured rock

model. However, it should be noted that the actual stress state ${\sigma_{ij}}^A$ differs from ${\sigma_{ij}}^{ini}$, because C_{ijkl} of the fractured rock model is more compliant than that of the intact rock. Therefore, we updated ${\varepsilon_{kl}}^A$ using a calculated C_{ijkl} (VTI) with Eq. (5) to satisfy ${\sigma_{ij}}^{ini} = 20$MPa, and then repeated the calculation. The calculation was iterated until ${\sigma_{ij}}^A$ became close enough to ${\sigma_{ij}}^{ini}$ (Fig. 2b). This isostress iteration process converged within the third iteration (Fig. S3). The final result for C_{ijkl} was then used for determining the initial input strain of the proceeding model. Similarly, we proceeded with the calculations towards the largest aperture model ($d = 0.2$ mm) by updating the input strain ${\varepsilon_{ij}}^A$ in each fracture aperture model such that ${\sigma_{ij}}^A = {\sigma_{ij}}^{ini} = 20$ MPa (Fig. 2c). This NSC process enabled us to simulate the isostress condition and minimize the gap between the two bounds obtained from the isostress and isostrain conditions, thereby providing reasonable changes in the stiffness tensors (Yamamoto et al., 1981).

Table 1. Physical properties used for the finite element modeling.

	Bulk modulus [GPa]	Shear modulus [GPa]	Density [kg/m^3]
Solid	59.5*	30.5*	2750
Fluid	2.25**	0**	994**

* Based on P- and S-wave velocity measurements under dry conditions and at a high confining pressure (200 MPa).

** For water at the standard state.

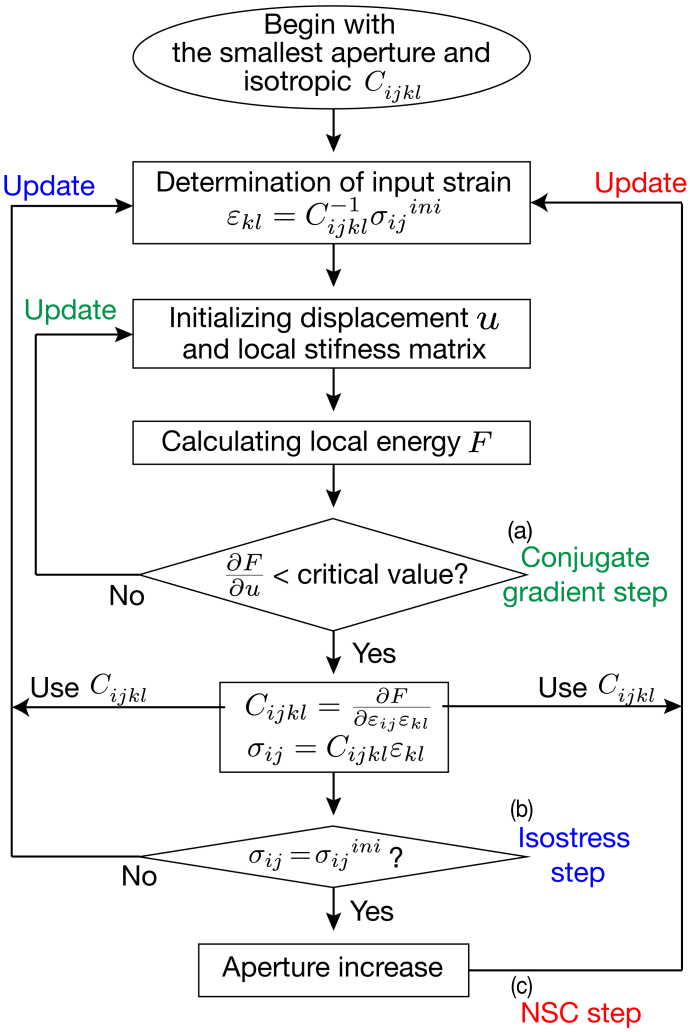

Figure 2. Flow diagram of the approach used for calculating the stiffness tensor by integrating the finite element and numerical self-consistent methods. The input strain for the finite element model was consecutively updated until the macroscopic stress became close to 20 MPa at each aperture condition.

3.4. Experimental verification

We verified the numerical results for the elastic wave velocity using experimental results. The experimental sample was prepared as a cylindrical specimen (35 mm in diameter and 70 mm long), in which the fracture plane was parallel to the central axis. After mapping the fracture surfaces as described in Section 3.1, the sample was restored to its original state. The P-wave velocity in the direction normal to the fracture plane was then measured by the pulse transmission method at eight effective normal stresses from $P_{\text{eff}} = 1$–15 MPa. The input

trigger of a pulse was set to a frequency of 250 kHz and amplitude of 10 Vp-p. Details of the experimental setup were described in Sawayama et al. (2018a).

The simulated velocity change of the experimental fracture was evaluated with our modified FEM approach. The aperture between the two surfaces in the digital model was adjusted such that the model had a simulated permeability equivalent to that measured in the experiments at each stress state (Sawayama et al., 2021b). The thickness was determined by matching with the measured fracture porosity in this sample (1.6% at atmospheric pressure; Sawayama et al., 2021b). The wavelength under our experimental conditions is at least ten times larger than the largest length of the estimated aperture (0.06 mm). It should also be noted that the experimental velocity change includes both velocity changes in the matrix and fracture associated with the elevated stress. Therefore, we modeled the changes in elastic constants in a matrix (K_m and μ_m) based on P- and S-wave velocities at elevated P_{eff} as $K_m = 0.128\ P_{\text{eff}} + 6.49$ and $\mu_{\text{m}} = 0.0048\ P_{\text{eff}} + 27.29$, based on an experiment on an intact andesite sample retrieved from the same borehole as the fractured sample.

4. Results

4.1. Elastic energy

Based on the 24 × 24 mm synthetic fracture, we calculated local distributions of stress, strain, and elastic energy with the FEM. Figure 3 shows the cross-sections of their local distributions with a 0.2 mm mean aperture. The vertical stress and strain (σ_{33} and ε_{33}) are normalized by their macroscopic values (${\sigma_{33}}^A$ and ${\varepsilon_{33}}^A$), whereas the local energy is normalized by the energy of the intact rock (E_0). The mean position of the fracture plane is located at the center of the model (5 mm in the z-direction). The stress and energy are mainly concentrated on the edges of the fracture asperity contacts (Fig. 3a), whereas the strain is accumulated inside the fracture (Fig. 3b). Notably, their anomalies converge near the fracture. Figure 4 shows the horizontal mean energy and corresponding cross-sections of the energy distributions. The peak of the energy is consistent with the mean fracture position. It is clearly evident that the energy is only localized at 3.5–6.5 mm in the vertical position (i.e., 1.5 mm from the mean fracture position). The energy anomaly disappears near the top (z = 1.0 mm) and bottom (z = 9.0 mm) of the model, indicating the model thickness was sufficiently large at the given aperture conditions.

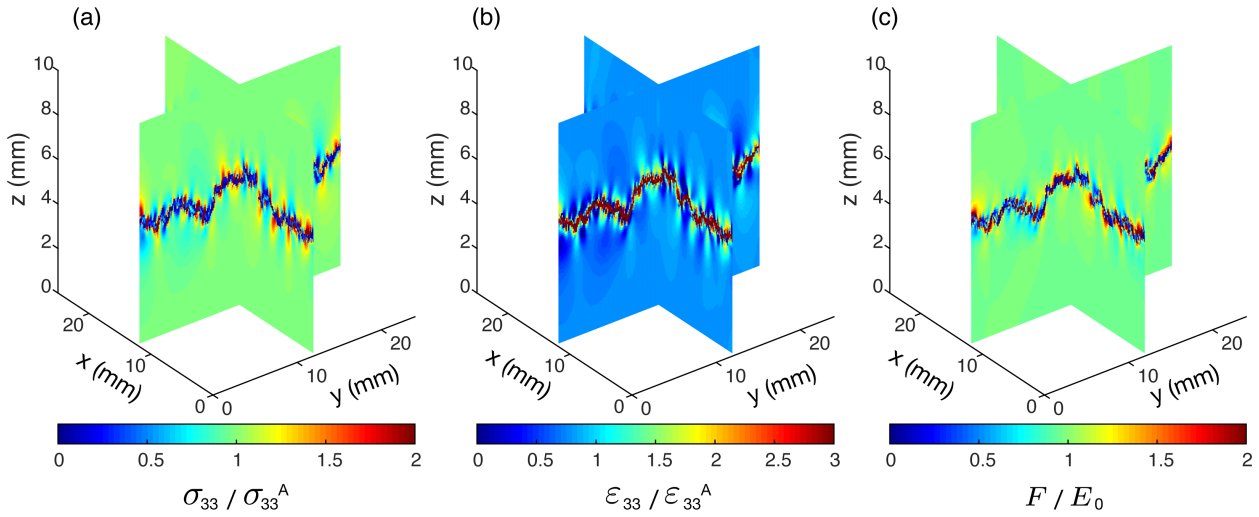

Figure 3. Local distribution of normalized values of the (a) vertical stress, (b) vertical strain, and (c) elastic energy of the 24 × 24 mm fractures at a 0.2 mm mean aperture.

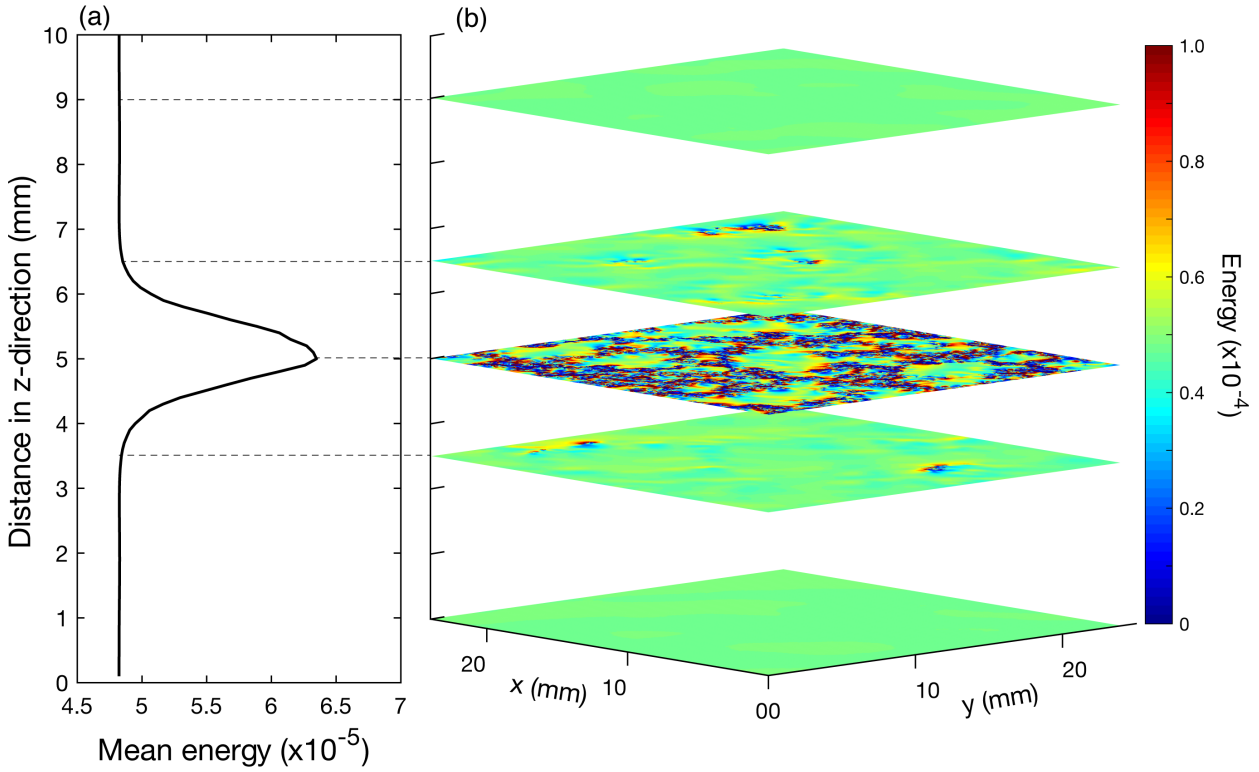

Figure 4. (a) Areal average of the elastic energy in the x–y-plane and (b) areal distribution of local elastic energy at 0.2 mm mean aperture.

The change in the elastic energy of the base model shows a non-linear increase with aperture opening (Fig. S4). Note that the energy change obtained with our approach was slightly larger than the result without updating the strain input, and this discrepancy became more significant as the aperture increased (Fig. S4a). Consequently, the conventional approach (i.e., the isostrain assumption) underestimated the velocity change due to the fracture aperture opening (Fig. S4b). In addition to the aperture change, the model thickness potentially affects the elastic energy. When the model thickness is larger, the energy anomaly near the fracture will be relatively smaller. We therefore analyzed the elastic energy when the thickness was twice that of the base model (i.e., 20 mm thickness). The relative energy changes of the 20-mm-thick model were smaller than those of the base model (Fig. S4c). Given that we adopted a periodic boundary in all directions, twice the model thickness is equivalent to half of the fracture density D_F (i.e., number of fractures per unit thickness). When two single-aligned fractures were embedded in the 20 mm thickness (i.e., the same D_F as the base model), both results showed good agreement (Fig. S4c).

4.2. Velocity changes with aperture opening

From the stiffness tensor determined from the elastic energy, P-wave velocity V_p and S-wave velocity V_s in the direction normal to the fracture plane were calculated as:

$$V_p = \sqrt{\frac{C_{3333}}{\rho}}, \quad V_s = \sqrt{\frac{C_{1212}}{\rho}}, \quad \#(8)$$

where ρ is the arithmetic average of densities of solid and pore water (Table 1). The resultant changes with aperture opening are plotted in Fig. 5 (a), and show the non-linear decrease of V_p and V_s. The change in V_s is slightly smaller than that of V_p, which is consistent with the numerical simulation and laboratory experiments on natural rock fractures (Cha et al., 2009; Sawayama et al., 2021a).

The phase velocities of the following three modes were also evaluated. The velocities of quasi-longitudinal (qP), quasi-shear (qS), and pure shear (SH) modes in transversely isotropic material along the z-axis are given as (Mavko et al., 2009):

$$V_{\mathrm{qP}}(\theta) = \sqrt{\frac{C_{1111}\sin^2\theta + C_{3333}\cos^2\theta + C_{1212} + \sqrt{M(\theta)}}{2\rho}}, \quad \#(9)$$

$$V_{\mathrm{qS}}(\theta) = \sqrt{\frac{C_{1111}\sin^2\theta + C_{3333}\cos^2\theta + C_{1212} - \sqrt{M(\theta)}}{2\rho}}, \quad \#(10)$$

$$V_{\mathrm{SH}}(\theta) = \sqrt{\frac{(C_{1111} - C_{1122})\sin^2\theta + 2C_{1212}\cos^2\theta}{2\rho}}, \quad \#(11)$$

where

$$M(\theta) = \left[(C_{1111} - C_{1212})\sin^2\theta - (C_{3333} - C_{1212})\cos^2\theta\right]^2 + (C_{1133} + C_{1212})^2 \sin^2\theta . \#(12)$$

θ is the angle between the wave vector and symmetry axis ($= 0$ for a propagation direction normal to the fracture plane), indicating $V_{\mathrm{qP}}(0) = V_p$ and $V_{\mathrm{qS}}(0) = V_{\mathrm{SH}}(0) = V_s$ in Eq. (8). The results are shown in Fig. 5b and c. The aperture effect on the velocity change is significant at $< 70^\circ$ (Fig. 5b). V_{qS} and V_{SH} show different trends, whereby V_{qS} is mostly faster than V_{SH}, but slower than V_{SH} at $\theta > 70^\circ$. This discrepancy between the two modes of S-waves reflects the angular dependence on shear wave anisotropy, which can be expressed as $(V_{\mathrm{qS}} - V_{\mathrm{SH}})/[(V_{\mathrm{qS}} + V_{\mathrm{SH}})/2]$ (Fig. 5d). Consequently, the anisotropy shows a peak at $= 40^\circ$, and the peak value increases with aperture opening. The peak angle has a similar value to that of a shale fracture, which will be $<45^\circ$ depending on the anisotropy of the material (Berryman, 2008).

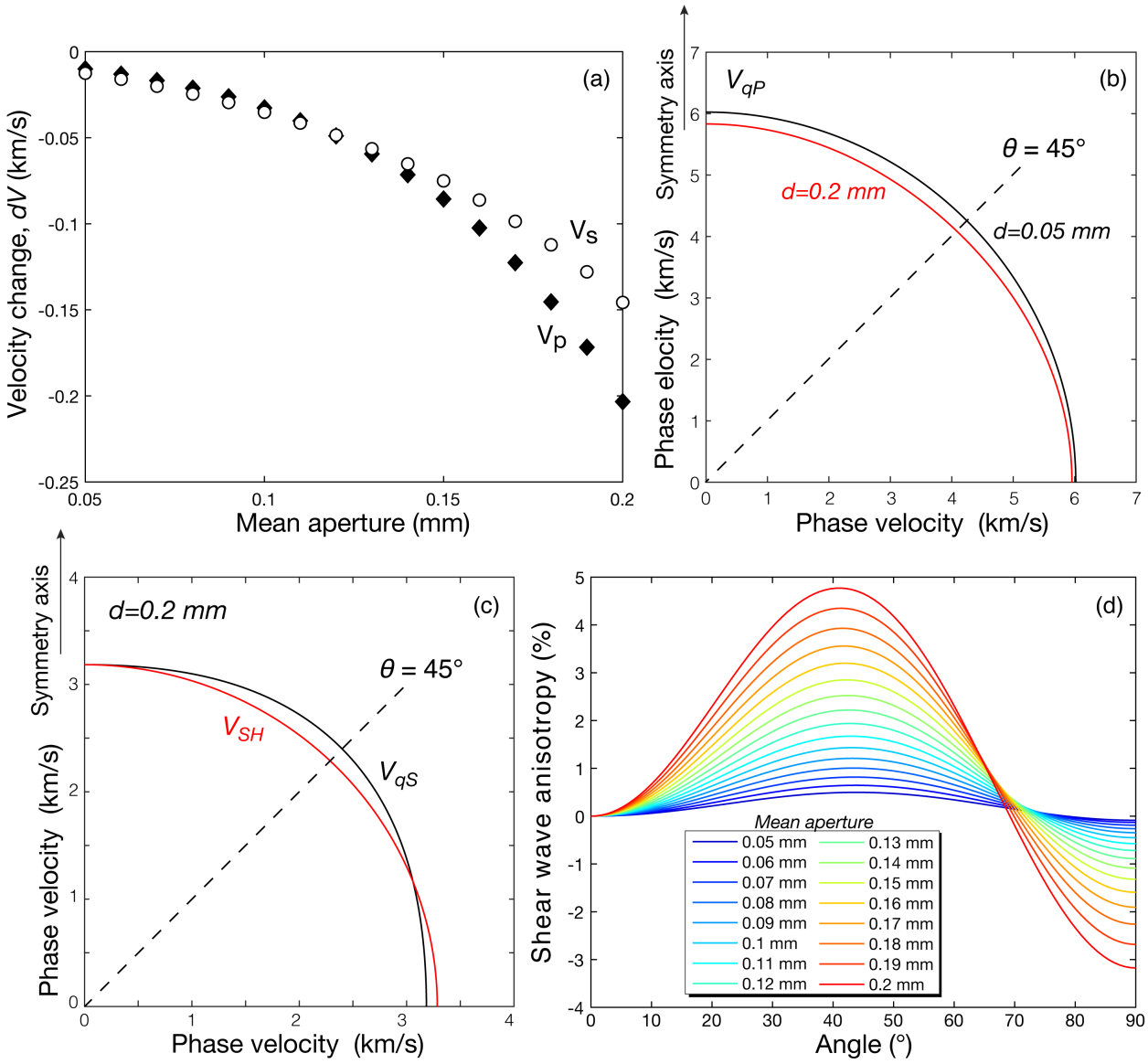

Figure 5. Plots showing the (a) P- and S-wave velocity in a direction perpendicular to the fracture plane as a function of the mean aperture, (b) angular phase velocity distributions for *qP* at 0.05 and 0.2 mm mean aperture, (c) angular phase velocity distributions for *qS* and *SH* waves, and (d) shear wave anisotropy as a function of the angle under various aperture conditions.

4.3. Fracture upscaling

We extended the calculations to different sizes of synthetic fractures (24, 48, and

96 mm) with five different random seeds. Figure 6 shows changes in V_p, V_s, and shear wave anisotropy versus the mean aperture at various fracture sizes and random seeds. These plots show there are no significant differences resulting from changes in the random seeds and fracture size, demonstrating both the repeatability of the simulations and the size-independent characteristics of the velocities in the simulated fractures. These size-independent characteristics suggest that fracture size does not strongly affect the velocity perturbation when the wavelength is much larger than the fracture.

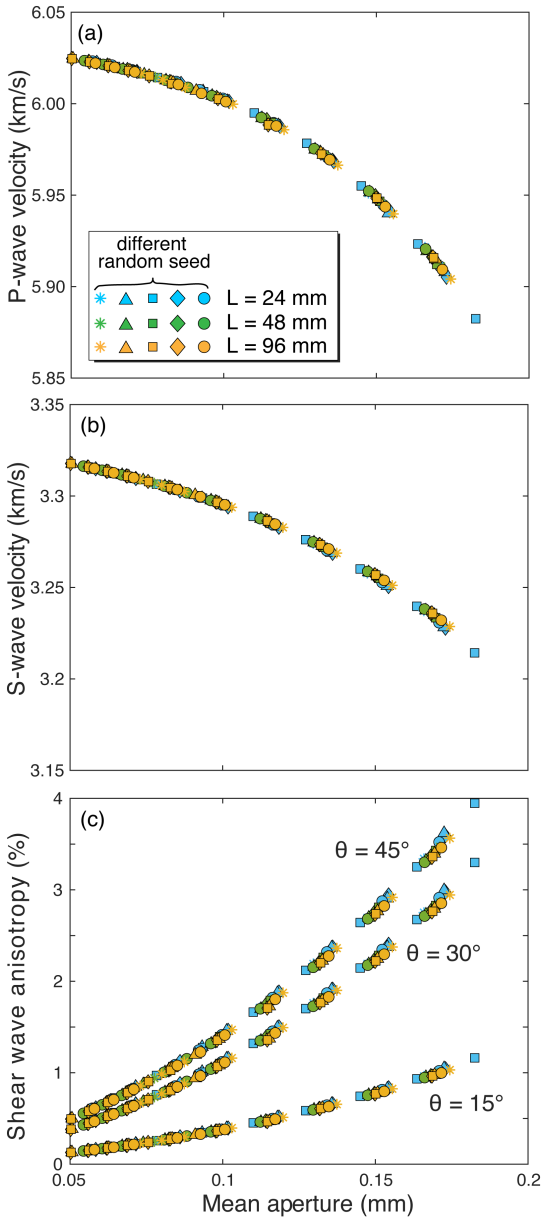

Figure 6. Changes in the (a) P-wave velocity, (b) S-wave velocity, and (c) shear wave anisotropy as functions of the mean aperture. Symbol shapes correspond to the different random seeds, and their colors correspond to the different fracture sizes. θ is the angle between the wave vector and symmetry axis ($= 0$ for a propagation direction perpendicular to the fracture plane).

4.4. Fracture density

Figure 7 shows changes in V_p, V_s, and shear wave anisotropy versus the mean aperture in a multi-fracture system. V_p and V_s clearly decrease with an increasing number of fractures, and this effect is prominent in larger aperture models (Fig. 7a and b). Shear wave anisotropy also shows a similar trend (Fig. 7c). Although we used a model having a 1.5 mm fracture spacing, the effect of the fracture spacing on V_p, V_s, and shear wave anisotropy was small (Fig. S5a–c). This is because the elastic energy was less sensitive to the fracture spacing, unless the fractures intersected (Fig. S5d). The same D_F model shows the same velocity and anisotropy trends regardless of the different model thicknesses (Fig. S6). These results indicate that the experimentally determined dependencies on both the number of fractures and rock thickness (e.g., Kurtuluş et al., 2012; Yang et al., 2019) are accounted for by considering the fracture density.

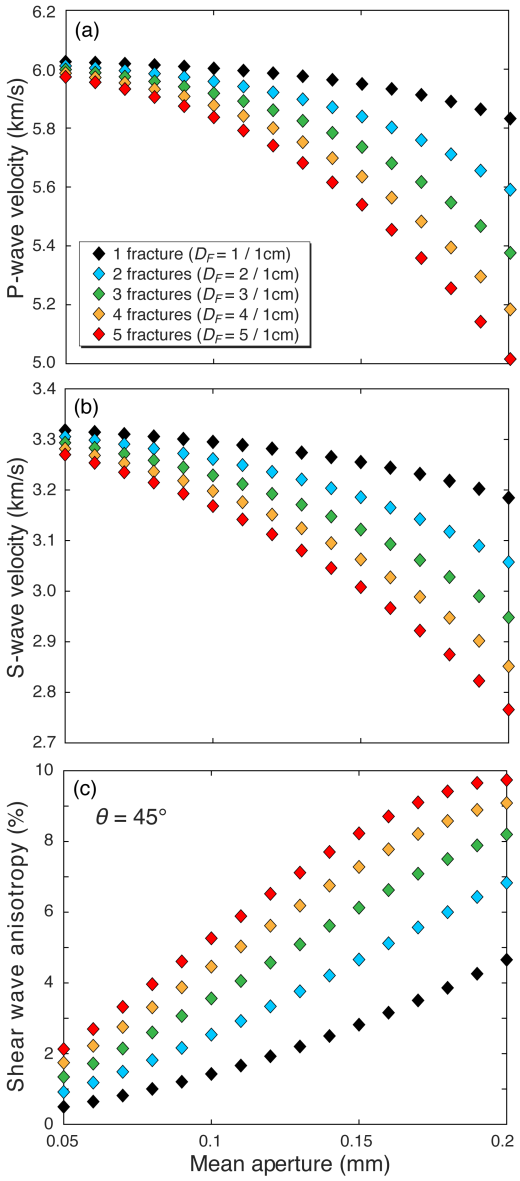

Figure 7. Changes in the (a) P-wave velocity, (b) S-wave velocity, and (c) shear wave anisotropy at an angle $\theta = 45^\circ$ as a function of the mean aperture. The symbol colors correspond to the different fracture densities.

4.5. Comparison of numerical and experimental results

The P-wave velocities obtained from our numerical approach were compared with experimental data. Figure 8 shows the P-wave velocities in the experiment and from the numerical approach. The raw data indicate that the numerical

results for the digital rock models of all fracture areas have a slightly lower velocity than the experimental values. This may be due to the mismatch between the numerical model and actual path area in the experimental setup, as the point-source input pulse in the experiment will have a smaller scope than the entire fracture plane. When the ray path is approximately straight, the propagating wave interacts with the medium inside a prolate spheroid, with a major axis that links the source and receiver transducers, which is known as the first Fresnel zone. The length of the minor axis of the spheroid r is given by (Spetzler & Snieder, 2004):

$$r = \sqrt{\frac{l}{2}}.\#(13)$$

where l and are the half-distance between the source and receiver transducers and the wavelength of the propagating P-wave, respectively. The experimental pulse frequency of 250 kHz yields r = 13.3 mm by assuming V_p = 5 km/s. We therefore constructed the digital rock model using 13.3 mm square-sized fracture from the experimental source position to undertake a further simulation. The updated simulation result is more like the experimental value (FZ in Fig. 8). A small discrepancy may arise from the gap between the estimated porosity or asperity contacts, based on the permeability, and actual values, as the velocity is more sensitive to these factors than the permeability (Sawayama et al., 2021a). Overall, the trends of the experimental results are consistent with the simulated velocity by incorporating the matrix velocity change and model fracture size according to the experimental ray path.

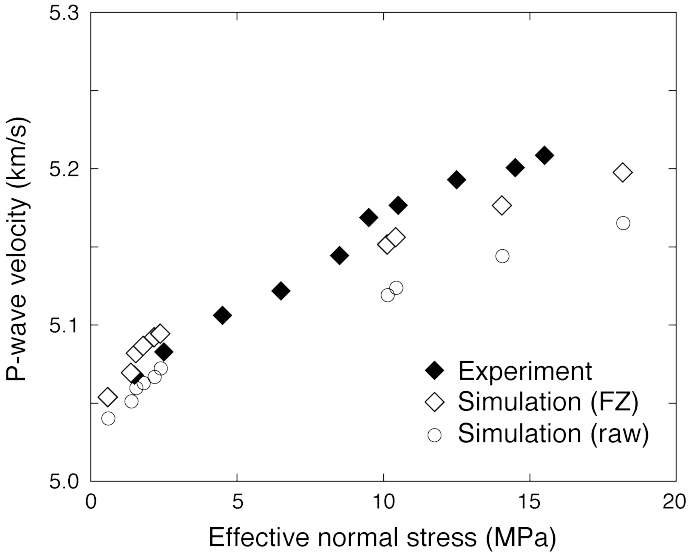

Figure 8. Experimental and simulated P-wave velocity with increasing effective normal stress. Solid and open symbols represent experimental and simulated

results, respectively. The raw and FZ simulation data are the P-wave velocity of the entire fracture plane and estimated first Fresnel zone, respectively.

5. Discussion and applications

We have demonstrated that the changes in elastic energy (and therefore the elastic wave velocity) of the fracture in Eshelby's model can be accounted for by the fracture aperture and density (Figs 5 and 7), which the volume fraction of an inclusion represents. The velocity in the direction normal to the fracture can be simply modeled as a horizontal layered structure comprising matrix and an inclusion. Assuming a long-wavelength limit, V_p is given by the effective medium theory (Mavko et al., 2009):

$$V_p = \sqrt{\frac{M}{\rho}}. \#(14)$$

Given that the fracture is filled with pore water, the effective P-wave modulus M $(K + 4/3\mu)$ is obtained from the Backus average:

$$\frac{1}{M} = \frac{1-f_w}{M_s} + \frac{f_w}{M_w}, \ \#(15)$$

where f_w is the volume fraction of pore water given by the ratio of the mean aperture to model thickness, and M_s and M_w are the P-wave modulus of the solid and pore water, respectively. The predicted V_p from Eq. (14) of our digital fracture at a mean aperture d = 0.2 mm yields 4.44 km/s, which is much smaller than the simulation result (Fig. 7a). Moreover, the simulation results show that the velocity at d = 0.2 mm and $D_F = 1$ cm^{-1} is much smaller than the velocity at d = 0.1 mm and $D_F = 2$ cm^{-1} (Fig. 7a), even though Eq. (14) yields the same V_p. In both cases, the simple effective medium theory will underestimate the velocity, indicating that f_w cannot account for the velocity change of mated fractures. As such, both the mean aperture and fracture density are essential for predicting the velocity of mated fractures. We therefore modeled the velocity changes as functions of aperture and fracture density. Figure 9 shows V_p and V_s normalized by the matrix velocity ($V_p{}^o$ = 6.04 km/s; $V_s{}^o$ = 3.33 km/s) as functions of aperture and fracture density. The colored surface in Fig. 9 represents the curve fitting results using the following models:

$$\frac{V_p}{V_p{}^o} = 1 - D_F \left(1.39d^2 - 0.136d + 5.90 \times 10^{-3}\right), \#(16)$$

$$\frac{V_s}{V_s{}^o} = 1 - D_F \left(0.952d^2 - 0.0277d + 2.98 \times 10^{-3}\right). \#(17)$$

The empirical model predictions are consistent with our simulation results in the base model (Fig. 9), and with a much wider range of D_F values for the 20 mm thickness model (Fig. S6). These empirical models imply that the elastic

wave velocity of the fractured rock mass can be accounted for by the superposition of a linear function of the fracture density and quadratic function of the aperture. A linear decrease in elastic wave velocity with fracture density has also been reported in some experimental studies (Kahraman, 2001; Kurtuluş et al., 2012; Yang et al., 2019). These studies observed different trends for the relationship depending on the rock samples, which might be related to the fracture characteristics (e.g., roughness, fractal dimensions, and mismatch length scale). These characteristics may also affect aperture-related velocity changes in a single mated fracture (Cha et al., 2009; Mohd-Nordin, 2016; Sawayama et al., 2021a). Future studies need to clarify the mechanism of determining the empirical parameters with respect to fracture geometry. Notably, the proposed empirical model allows us to extrapolate the aperture–velocity relationship for a single fracture to multiple fractures comprising a vertical series of the same fractal surfaces.

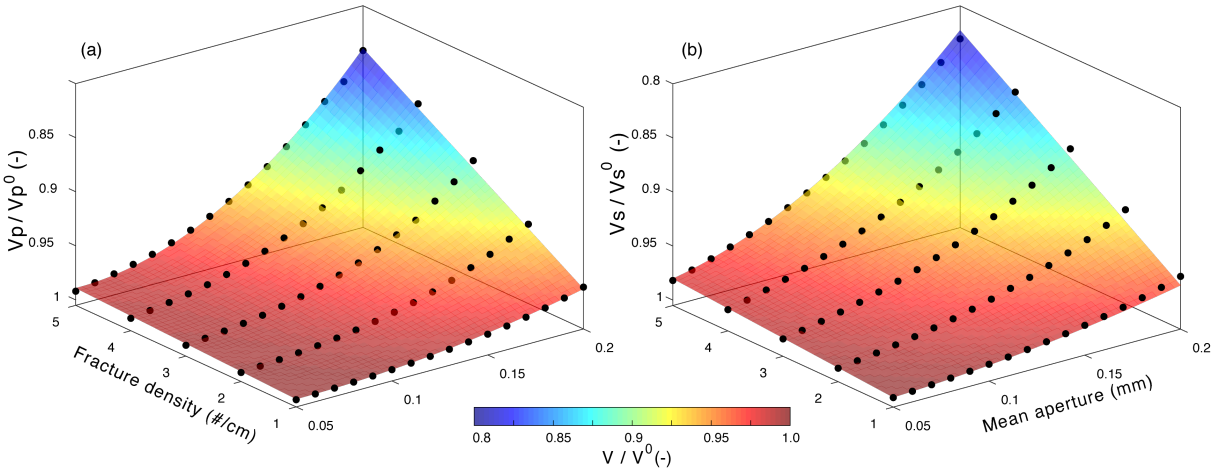

Figure 9 Curve fitting results of the (a) P-wave velocity and (b) S-wave velocity normalized to the matrix values. The plots show the simulation results and the color surfaces represent the curve fitting model based on Eqs (16) and (17).

One application of our finding is that it is possible to correlate the elastic wave velocity with fracture permeability with respect to the aperture and fracture density. When the number of fractured layers N_F having the same mean aperture d is vertically accumulated in a unit volume, the total fracture permeability k can be simply given by $k = (N_F d)^2/12$, while the elastic wave velocities can be derived from the empirical models (Eqs (16) and (17)). The predicted relationship between fracture permeability and elastic wave velocity (i.e., the k–V relationship) is shown in Fig. 10. The simulation results for the permeability (Sawayama et al., 2021b) and elastic wave velocities (Fig. 9) using the same digital fracture models are also plotted, and are consistent with the predictions and show no significant changes with fracture size. Both the V_p and V_s changes are larger at higher permeability ($\log(k) < 10.8$ at N_F=1), whereas they are almost

constant at lower permeability. This reflects the different mechanisms underlying both properties; the velocity change becomes small after a large fraction of the asperities become in contact, while permeability continuously decreases with increasing contact area (Sawayama et al., 2021a). Fracture density changes the k–V relationship, and changes in velocity and permeability at higher D_F are much larger than those at lower D_F. This suggests that the direct prediction of permeability from the observed velocity might be difficult in a natural setting, unless D_F is known.

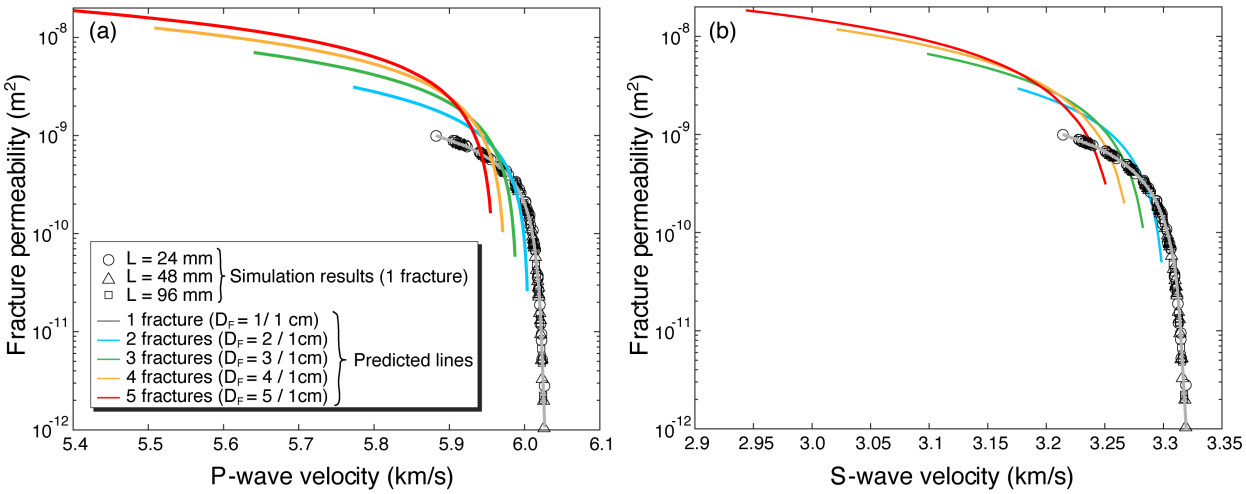

Figure 10. Plots of the fracture permeability versus (a) P-wave velocity and (b) S-wave velocity. The plots show the simulation results and the symbol shapes represent different fracture length sizes. The colored lines show the predicted relationships of different fracture densities extrapolated from the results of the single fracture model.

In contrast, the offset of the k–V relationship can be neglected by focusing on the relative changes in these properties for monitoring. The k–V relationship is thus normalized by the reference values. We used $d = 0.065$ mm as the reference value, where the dominant flow channel is disconnected (Sawayama et al., 2021b). Consequently, the relative k–V relationship shows clear linearity in linear coordinates, and the trend depends on fracture density (Fig. 11). Therefore, the k–V relationship can be modeled as follows:

$$\frac{k}{k'} = \frac{\alpha_p}{D_F}\frac{V_p^{'} - V_p}{V_p^{'}}, \quad \#(18)$$

$$\frac{k}{k'} = \frac{\alpha_s}{D_F}\frac{V_s^{'} - V_s}{V_s^{'}}, \quad \#(19)$$

where k', $V_p^{'}$, and $V_s^{'}$ are arbitrary reference values of the permeability, and P- and S-wave velocities, respectively. The empirical parameters α_p and α_s

represent the linearity of the k–V_p and k–V_s relationships for a single fracture, respectively. The predicted lines using $\alpha_p = 3000$ and $\alpha_s = 2500$ are also shown in Fig. 11. The predicted k–V_p relationship is consistent with the simulation results for $k/k' < 30$ (Fig. 11a), whereas the trend deviates from the simulation results at $k/k' > 30$. This deviation point corresponds to $d = 0.13$ mm (or 25% of the contact area), suggesting that changes in V_p become small when the fracture contact is weaker than this threshold. This trend for $k/k' > 30$ shows good agreement when $\alpha_p = 2200$ (Fig. 11a). Although no studies have correlated the fracture permeability and velocity, some experimental studies (e.g., Alam et al., 2011; Prasad, 2003) have found that the trend of the k–V_p relationship for a porous rock varies with the lithology, which may be due to pore and grain features (e.g., tortuosity, specific surface area, impurities, and clay contents). Our results revealed that the trend of the k–V_p relationship for a fracture is strongly related to D_F, and will also change according to the fracture contact state. In contrast, the trend of the k–V_s relationship is irrelative to the contact state, and constant in fractures with the same fractal characteristics and D_F (Fig. 11b). Although the empirical parameter α can vary with fracture types, it can be determined from the k–V relationship for a single fracture. This finding implies that investigations of small-scale single fractures and the k–V relationship can be extrapolated to multiple fractures in natural settings. Therefore, velocity monitoring (especially V_s) can potentially evaluate changes in fracture permeability.

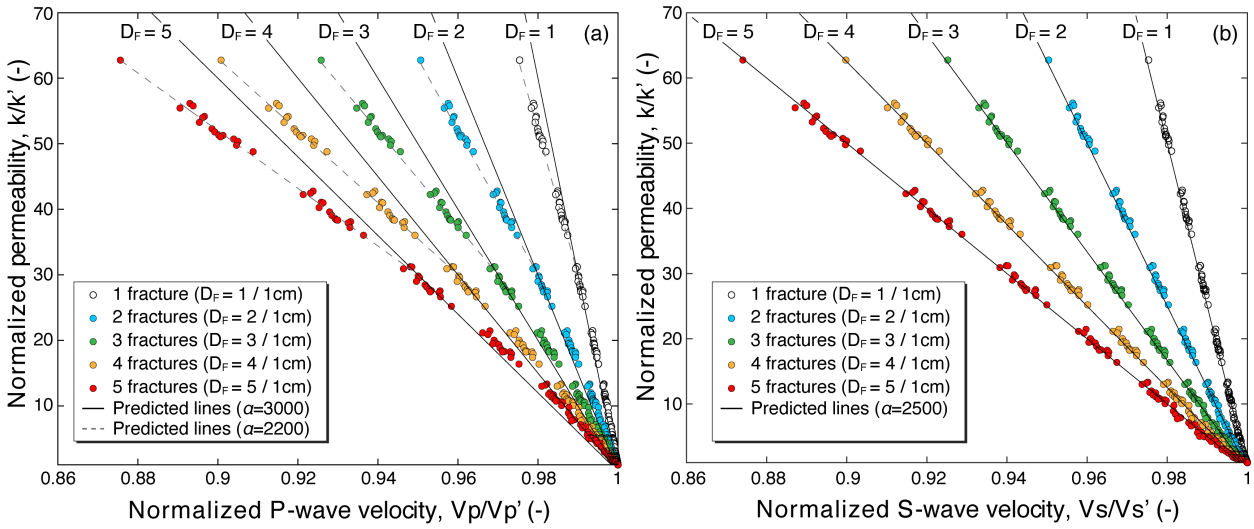

Figure 11. Plots of permeability versus (a) P-wave velocity and (b) S-wave velocity normalized to the reference values (see the text for details). The symbol colors represent the fracture densities and the lines denote the predicted relationships based on Eqs (18) and (19).

Although the presented digital rock models are mated fractures based on

isotropic surfaces, it should be noted that permeability enhancement by hydraulic stimulation is triggered not only by joint openings but also by shear slip (e.g., Rinaldi & Rutqvist, 2019). Future work should extend this approach to solving for the stiffness tensor in the orthorhombic case (e.g., sheared fractures) to confirm the limitations of the proposed formulae. Another limitation of the formulae arises from the assumption that there is no matrix velocity change. It is known that the velocity change at elevated pressure is significant at higher crack density (i.e., lower stress), but is smaller at lower crack density (i.e., higher stress). Such a pressure effect on velocity change will be smaller if cracks are filled with water and have low aspect ratios (Nur & Simmons, 1969; O'Connnell & Budiansky, 1974; Hadley, 1976; Meglis et al., 1996; Paterson & Wang, 2005; Watanabe & Higuchi, 2015). Therefore, the proposed empirical model could be used for rocks with a low crack aspect ratio (e.g., volcanic rocks) or under higher crustal stress conditions, which has negligibly small changes in matrix velocity. Given that our approach can incorporate matrix velocity changes when experimental data are available (Fig. 8), our method can be extended to rocks with a high crack aspect ratio (e.g., granite). Moreover, the method needs to be tested further for size dependencies, because the studied experimental fracture was much smaller than natural fractures. For example, a test site of the enhanced geothermal system has a kilometer-scale fracture (e.g., Didana et al., 2017). Although our study adopted a zero frequency assumption for the velocity calculation, the scaling effect on velocity can be addressed by considering the ratio of the finite wavelengths and fracture size (Mavko et al., 2009). Because finite-difference time-domain modeling of wave fields in fractured media requires more complex assumptions, such as fracture compliance (Bakulin et al., 2000; Minato & Ghose, 2016; Pyrak-Nolte et al., 1990), future studies need to further investigate the scale dependency of velocity using this technique.

4. Conclusions

We developed a method for calculating the hexagonal form of the stiffness tensor based on internal energy calculations, and investigated the changes in elastic wave velocities and shear wave anisotropy with aperture opening. Simulated local elastic energy revealed that the interaction energy converged within 1.5 mm of the mean fracture position, and was insignificant unless the fractures intersected. The energetic approach integrating FEM and NSC methods identified the aperture–velocity relationship and reproduced the experimental results. Further calculations using digital fractures with various sizes and densities showed that the elastic wave velocity can be accounted for by the superposition of a linear function of the fracture density and quadratic function of the aperture, and is independent of the fracture size. We also showed that the k–V relationship is independent of fracture size, but dependent on fracture density. In contrast, the k–V relationship shows a clear linearity with fracture density when the offset is normalized by arbitrary reference values. Although further study is needed to confirm the empirical parameters determining the slope of this relationship, our results indicate that laboratory-scale fracture properties for a single fracture can

be extended to multiple fractures. Our findings indicate that temporal changes in seismic properties might be used for monitoring fracture flow.

Acknowledgments

Authors acknowledge I. Katayama, K. Yamada, T. Ishibashi, J. Nishijima, and K. Kitamura for technical support and discussion. This study was supported in part by the Japan Society for the Promotion of Science (JSPS) through a Grant-in-Aid for JSPS Fellows, JP19J10125 (to K.S.), Grant-in-Aid for Young Scientists, JP19K15100 (to F.J.) and Grant-in-Aid for Challenging Exploratory Research, JP20K20948 (to T.T.). T.I., T.T., F.J., and O.N. are also grateful for the support of the International Institute for Carbon Neutral Energy Research (I2CNER), which is sponsored by the World Premier International Research Center Initiative of the Ministry of Education, Culture, Sports, Science and Technology (MEXT), Japan. The fracture data is from Sawayama et al. (2021b). All results are included in the Supporting Information.

References

Alam, M. M., Fabricius, I. L., & Prasad, M. (2011). Permeability prediction in chalks. *AAPG Bulletin*, *95*(11), 1991–2014. https://doi.org/10.1306/03011110172

Andrä, H., Combaret, N., Dvorkin, J., Glatt, E., Han, J., Kabel, M., et al. (2013). Digital rock physics benchmarks—part II: Computing effective properties. *Computers & Geosciences*, *50*, 33–43. https://doi.org/10.1016/j.cageo.2012.09.008

Arns, C. H., Knackstedt, M. A., Pinczewski, W. V., & Garboczi, E. J. (2002). Computation of linear elastic properties from microtomographic images: Methodology and agreement between theory and experiment. *Geophysics*, *67*(5), 1396–1405. https://doi.org/10.1190/1.1512785

Bakulin, A., Grechka, V., & Tsvankin, I. (2000). Estimation of fracture parameters from reflection seismic data—Part II: Fractured models with orthorhombic symmetry. *Geophysics*, *65*(6), 1803–1817. https://doi.org/10.1190/1.1444864

Berryman, J. G. (2008). Exact seismic velocities for transversely isotropic media and extended Thomsen formulas for stronger anisotropies. *Geophysics*, *73*(1), D1–D10. https://doi.org/10.1190/1.2813433

Brown, S. R. (1995). Simple mathematical model of a rough fracture. *Journal of Geophysical Research: Solid Earth*, *100*(B4), 5941–5952. https://doi.org/10.1029/94JB03262

Brenguier, F., Campillo, M., Hadziioannou, C., Shapiro, N. M., Nadeau, R. M., & Larose, E. (2008). Postseismic Relaxation Along the San Andreas Fault at Parkfield from Continuous Seismological Observations. *Science*, *321*(5895), 1478–1481. https://doi.org/10.1126/science.1160943

Cha, M., Cho, G.-C., & Santamarina, J. C. (2009). Long-wavelength P-wave and S-wave propagation in jointed rock masses. *Geophysics*, *74*(5), E205–E214. https://doi.org/10.1190/1.3196240

Didana, Y. L., Heinson, G., Thiel, S., & Krieger, L. (2017). Magnetotelluric monitoring of permeability enhancement at enhanced geothermal system project. *Geothermics*, *66*, 23–38. https://doi.org/10.1016/j.geothermics.2016.11.005

Eshelby, J. D. (1957). The determination of the elastic field of an ellipsoidal inclusion, and related problems. *Proceedings of the Royal Society of London. Series A. Mathematical and Physical Sciences*, *241*(1226), 376–396. https://doi.org/10.1098/rspa.1957.0133

Garboczi, E.J., (1998). Finite element and finite difference programs for computing the linear electric and elastic properties of digital image of random materials. *Natl. Inst. Stand. Technol. Interag. Rep.*, 6269.

Guéguen, Y., & Boutéca, M. (2004). *Mechanics of Fluid-Saturated Rocks*, Cambridge, MA: Academic Press.

Guéguen, Y., & Palciauskas, V. (1994). *Introduction to the physics of rocks*, Princeton, NJ: Princeton University Press.

Hadley, K. (1976). Comparison of calculated and observed crack densities and seismic velocities in westerly granite. *Journal of Geophysical Research*, *81*(20), 3484–3494. https://doi.org/10.1029/JB081i020p03484

Ikeda, T., & Tsuji, T. (2018). Temporal change in seismic velocity associated with an offshore MW 5.9 Off-Mie earthquake in the Nankai subduction zone from ambient noise cross-correlation. *Progress in Earth and Planetary Science*, *5*(1), 62. https://doi.org/10.1186/s40645-018-0211-8

Ishibashi, T., Watanabe, N., Hirano, N., Okamoto, A., & Tsuchiya, N. (2015). Beyond-laboratory-scale prediction for channeling flows through subsurface rock fractures with heterogeneous aperture distributions revealed by laboratory evaluation. *Journal of Geophysical Research: Solid Earth*, *120*(1), 106–124. https://doi.org/10.1002/2014JB011555

Kahraman, S. (2001). A correlation between P-wave velocity, number of joints and Schmidt hammer rebound number. *International Journal of Rock Mechanics and Mining Sciences*, *38*(5), 729–733. https://doi.org/10.1016/S1365-1609(01)00034-X

Kurtuluş, C., Üçkardeş, M., Sarı, U., & Onur Güner, Ş. (2012). Experimental studies in wave propagation across a jointed rock mass. *Bulletin of Engineering Geology and the Environment*, *71*(2), 231–234. https://doi.org/10.1007/s10064-011-0392-5

Le Ravalec, M., & Guéguen, Y. (1996a). High- and low-frequency elastic moduli for a saturated porous/cracked rock-Differential self-consistent and poroelastic theories. *Geophysics*, *61*(4), 1080–1094. https://doi.org/10.1190/1.1444029

Le Ravalec, M., Guéguen, Y., & Chelidze, T. (1996b). Elastic wave velocities in partially saturated rocks: Saturation hysteresis. *Journal of Geophysical Research: Solid Earth*, *101*(B1), 837–844. https://doi.org/10.1029/95JB02879

Manga, M., Beresnev, I., Brodsky, E. E., Elkhoury, J. E., Elsworth, D., Ingebritsen, S. E., … Wang, C.-Y. (2012). Changes in permeability caused by transient stresses: Field observations, experiments, and mechanisms. *Reviews of Geophysics*, *50*(2). https://doi.org/10.1029/2011RG000382

Matsuki, K., Chida, Y., Sakaguchi, K., & Glover, P. W. J. (2006). Size effect on aperture and permeability of a fracture as estimated in large synthetic fractures. *International Journal of Rock Mechanics and Mining Sciences*, *43*(5), 726–755. https://doi.org/10.1016/j.ijrmms.2005.12.001

Mavko, G., Mukerji, T. & Dvorkin, J. (2009). *The Rock Physics Handbook: Tools for Seismic Analysis of Porous Media.* 2nd ed., Cambridge, U.K.: Cambridge University Press.

Meglis, I. L., Greenfield, R. J., Engelder, T., & Graham, E. K. (1996). Pressure dependence of velocity and attenuation and its relationship to crack closure in crystalline rocks. *Journal of Geophysical Research: Solid Earth*, *101*(B8), 17523–17533. https://doi.org/10.1029/96JB00107

Minato, S., & Ghose, R. (2016). Enhanced characterization of fracture compliance heterogeneity using multiple reflections and data-driven Green's function retrieval. *Journal of Geophysical Research: Solid Earth*, *121*(4), 2813–2836. https://doi.org/10.1002/2015JB012587

Mohd-Nordin, M. M., Song, K.-I., Kim, D., & Chang, I. (2016). Evolution of Joint Roughness Degradation from Cyclic Loading and Its Effect on the Elastic Wave Velocity. *Rock Mechanics and Rock Engineering*, *49*(8), 3363–3370. https://doi.org/10.1007/s00603-015-0879-7

Nara, Y., Meredith, P. G., Yoneda, T., & Kaneko, K. (2011). Influence of macro-fractures and micro-fractures on permeability and elastic wave velocities in basalt at elevated pressure. *Tectonophysics*, *503*(1–2), 52–59. https://doi.org/10.1016/j.tecto.2010.09.027

Nimiya, H., Ikeda, T., & Tsuji, T. (2017). Spatial and temporal seismic velocity changes on Kyushu Island during the 2016 Kumamoto earthquake. *Science Advances*, *3*(11), e1700813. https://doi.org/10.1126/sciadv.1700813

Nishizawa, O. (1982). Seismic velocity anisotropy in a medium containing oriented cracks-transversely isotropic case, *Journal of Physics of the Earth*, *30*, 331–347. https://doi.org/10.4294/jpe1952.30.331

Nishizawa, O., & Kanagawa, K. (2010). Seismic velocity anisotropy of phyllosilicate-rich rocks: characteristics inferred from experimental and crack-model studies of biotite-rich schist. *Geophysical Journal International*, *182*(1), 375–388. https://doi.org/10.1111/j.1365-246X.2010.04614.x

Nolte, D. D., Pyrak-Nolte, L. J., & Cook, N. G. W. (1989). The fractal geometry of flow paths in natural fractures in rock and the approach to percolation. *Pure and Applied Geophysics*, *131*(1–2), 111–138. https://doi.org/10.1007/BF00874483

Nur, A., & Simmons, G. (1969). The effect of saturation on velocity in low porosity rocks. *Earth and Planetary Science Letters*, *7*(2), 183–193. https://doi.org/10.1016/0012-821X(69)90035-1

O'Connell, R. J., & Budiansky, B. (1974). Seismic velocities in dry and saturated cracked solids. *Journal of Geophysical Research*, *79*(35), 5412–5426. https://doi.org/10.1029/JB079i035p05412

Paterson, M. S. & Wong, T. (2005). *Experimental Rock Deformation: The Brittle Field*. 2nd ed., New York, NY: Springer-Verlag.

Prasad, M. (2003). Velocity-permeability relations within hydraulic units. *Geophysics*, *68*(1), 108–117. https://doi.org/10.1190/1.1543198

Pyrak-Nolte, L. J., Myer, L. R., & Cook, N. G. W. (1990). Transmission of seismic waves across single natural fractures. *Journal of Geophysical Research*, *95*(B6), 8617–8638. https://doi.org/10.1029/JB095iB06p08617

Pyrak-Nolte, L. J., & Nolte, D. D. (2016). Approaching a universal scaling relationship between fracture stiffness and fluid flow. *Nature Communications*, *7*(1), 10663. https://doi.org/10.1038/ncomms10663

Rinaldi, A. P., & Rutqvist, J. (2019). Joint opening or hydroshearing? Analyzing a fracture zone stimulation at Fenton Hill. *Geothermics*, *77*, 83–98. https://doi.org/10.1016/j.geothermics.2018.08.006

Sain, R., Mukerji, T., & Mavko, G. (2014). How computational rock-physics tools can be used to simulate geologic processes, understand pore-scale heterogeneity, and refine theoretical models. *The Leading Edge*, *33*(3), 324–334. https://doi.org/10.1190/tle33030324.1

Sánchez-Pastor, P., Obermann, A., Schimmel, M., Weemstra, C., Verdel, A., & Jousset, P. (2019). Short- and Long-Term Variations in the Reykjanes Geothermal Reservoir From Seismic Noise Interferometry. *Geophysical Research Letters*, *46*(11), 5788–5798. https://doi.org/10.1029/2019GL082352

Sawayama, K., Ishibashi, T., Jiang, F., Tsuji, T., & Fujimitsu, Y. (2021a). Relating Hydraulic–Electrical–Elastic Properties of Natural Rock Fractures at Elevated Stress and Associated Transient Changes of Fracture Flow. *Rock Mechanics and Rock Engineering*, *54*(5), 2145–2164. https://doi.org/10.1007/s00603-021-02391-5

Sawayama, K., Ishibashi, T., Jiang, F., Tsuji, T., Nishizawa, O., & Fujimitsu, Y. (2021b). Scale-independent relationship between permeability and resistivity in mated fractures with natural rough surfaces. *Geothermics*, *94*, 102065. https://doi.org/10.1016/j.geothermics.2021.102065

Sawayama, K., Kitamura, K., & Fujimitsu, Y. (2018). Laboratory measurements on electric and elastic properties of fractured geothermal reservoir rocks under simulated EGS conditions. *GRC Transactions*, *42*, 2459–2475.

Sibson, R. H., Robert, F., & Poulsen, K. H. (1988). High-angle reverse faults, fluid-pressure cycling, and mesothermal gold-quartz deposits. *Geology, 16*(6), 551–555, https://doi.org/10.1130/0091-7613(1988)016<0551:HARFFP>2.3.CO;2.

Spetzler, J., & Snieder, R. (2004). The Fresnel volume and transmitted waves. *Geophysics*, *69*(3), 653–663. https://doi.org/10.1190/1.1759451

Taira, T., Nayak, A., Brenguier, F., & Manga, M. (2018). Monitoring reservoir response to earthquakes and fluid extraction, Salton Sea geothermal field, California. *Science Advances*, *4*(1), e1701536. https://doi.org/10.1126/sciadv.1701536

Wang, L., & Cardenas, M. B. (2016). Development of an empirical model relating permeability and specific stiffness for rough fractures from numerical deformation experiments. *Journal of Geophysical Research: Solid Earth*, *121*(7), 4977–4989. https://doi.org/10.1002/2016JB013004

Watanabe, T., & Higuchi, A. (2015). Simultaneous measurements of elastic wave velocities and electrical conductivity in a brine-saturated granitic rock under confining pressures and their implication for interpretation of geophysical observations. *Progress in Earth and Planetary Science*, *2*(1), 37. https://doi.org/10.1186/s40645-015-0067-0

Witherspoon, P. A., Wang, J. S. Y., Iwai, K., & Gale, J. E. (1980). Validity of Cubic Law for fluid flow in a deformable rock fracture. *Water Resources Research*, *16*(6), 1016–1024. https://doi.org/10.1029/WR016i006p01016

Yang, H., Duan, H. F., & Zhu, J. B. (2019). Ultrasonic P-wave propagation through water-filled rock joint: An experimental investigation. *Journal of Applied Geophysics*, *169*, 1–14. https://doi.org/10.1016/j.jappgeo.2019.06.014

Yamamoto, K., Kosuga, M., & Hirasawa, T. (1981). A theoretical method for determination of effective elastic constants of isotropic composite. *The science reports of the Tohoku University. Fifth series, Tohoku geophysical journal,* 28(1), 47-67.